

The performance of 2D array detectors for light sheet based fluorescence correlation spectroscopy

Anand Pratap Singh,^{1,†} Jan Wolfgang Krieger,^{2,†} Jan Buchholz,²
Edoardo Charbon,³ Jörg Langowski,² and Thorsten Wohland^{1,*}

¹ *Departments of Biological Sciences and Chemistry and NUS Centre for Bio-Imaging Sciences, National University of Singapore, 14 Science Drive 4, 117557, Singapore*

² *German Cancer Research Centre (DKFZ), Biophysics of Macromolecules, Im Neuenheimer Feld 580, D-69120 Heidelberg, Germany*

³ *Technische Universiteit Delft, Mekelweg 4, 2628 CD Delft, The Netherlands*

[†] *Anand Pratap Singh and Jan Wolfgang Krieger contributed equally to this work.*

^{*} dbswt@nus.edu.sg

Abstract: Single plane illumination microscopy based fluorescence correlation spectroscopy (SPIM-FCS) is a new method for imaging FCS in 3D samples, providing diffusion coefficients, transport, flow velocities and concentrations in an imaging mode. SPIM-FCS records correlation functions over a whole plane in a sample, which requires array detectors for recording the fluorescence signal. Several types of image sensors are suitable for FCS. They differ in properties such as effective area per pixel, quantum efficiency, noise level and read-out speed. Here we compare the performance of several low light array detectors based on three different technologies: (1) Single-photon avalanche diode (SPAD) arrays, (2) passive-pixel electron multiplying charge coupled device (EMCCD) and (3) active-pixel scientific-grade complementary metal oxide semiconductor cameras (sCMOS). We discuss the influence of the detector characteristics on the effective FCS observation volume, and demonstrate that light sheet based SPIM-FCS provides absolute diffusion coefficients. This is verified by parallel measurements with confocal FCS, single particle tracking (SPT), and the determination of concentration gradients in space and time. While EMCCD cameras have a temporal resolution in the millisecond range, sCMOS cameras and SPAD arrays can extend the time resolution of SPIM-FCS down to 10 μ s or lower.

© 2013 Optical Society of America

OCIS codes: (180.2520) Fluorescence microscopy; (180.6900) Three-dimensional microscopy; (300.6280) Spectroscopy, fluorescence and luminescence; (040.0040) Detectors; (040.1240) Arrays; (040.1345) Avalanche photodiodes (APDs); (040.1490) Cameras.

References and links

1. K. M. Berland, P. T. So, and E. Gratton, "Two-photon fluorescence correlation spectroscopy: method and application to the intracellular environment," *Biophys. J.* **68**, 694–701 (1995).
2. P. Schwille, U. Haupts, S. Maiti, and W. W. Webb, "Molecular dynamics in living cells observed by fluorescence correlation spectroscopy with one- and two-photon excitation," *Biophys. J.* **77**, 2251–2265 (1999).
3. R. Brock, G. Vámosi, G. Vereb, and T. M. Jovin, "Rapid characterization of green fluorescent protein fusion proteins on the molecular and cellular level by fluorescence correlation microscopy," *Proc. Natl. Acad. Sci. U.S.A.* **96**, 10123–10128 (1999).

4. M. Wachsmuth, W. Waldeck, and J. Langowski, "Anomalous diffusion of fluorescent probes inside living cell nuclei investigated by spatially-resolved fluorescence correlation spectroscopy," *J. Mol. Biol.* **298**, 677–689 (2000).
5. R. H. Köhler, P. Schwille, W. W. Webb, and M. R. Hanson, "Active protein transport through plastid tubules: velocity quantified by fluorescence correlation spectroscopy," *J. Cell Sci.* **113**, 3921–3930 (2000).
6. X. Pan, H. Yu, X. Shi, V. Korzh, and T. Wohland, "Characterization of flow direction in microchannels and zebrafish blood vessels by scanning fluorescence correlation spectroscopy," *J. Biomed. Opt.* **12**, 014034 (2007).
7. X. Shi, Y. H. Foo, T. Sudaharan, S. W. Chong, V. Korzh, S. Ahmed, and T. Wohland, "Determination of dissociation constants in living zebrafish embryos with single wavelength fluorescence cross-correlation spectroscopy," *Biophys. J.* **97**, 678–786 (2009).
8. X. Shi, L. S. Teo, X. Pan, S. W. Chong, R. Kraut, V. Korzh, and T. Wohland, "Probing events with single molecule sensitivity in zebrafish and *Drosophila* embryos by fluorescence correlation spectroscopy," *Dev. Dyn.* **238**, 3156–3167 (2009).
9. D. Magde, E. Elson, W. Webb, and W. W. Magde, Douglas, Elliot Elson, "Thermodynamic fluctuations in a reacting system-measurement by fluorescence correlation spectroscopy," *Phy. Rev. Lett.* **29**, 705–708 (1972).
10. R. Rigler, U. Mets, J. Widengren, and P. Kask, "Fluorescence correlation spectroscopy with high count rate and low background: analysis of translational diffusion," *Eur. Biophys. J.* **22**, 169–175 (1993).
11. H. Blom, M. Johansson, A. S. Hedman, L. Lundberg, A. Hanning, S. Hård, and R. Rigler, "Parallel fluorescence detection of single biomolecules in microarrays by a diffractive-optical-designed 2 x 2 fan-out element," *Appl. Opt.* **41**, 3336 (2002).
12. M. Gösch, A. Serov, T. Anhut, T. Lasser, A. Rochas, P.-A. Besse, R. S. Popovic, H. Blom, and R. Rigler, "Parallel single molecule detection with a fully integrated single-photon 2x2 CMOS detector array," *J. Biomed. Opt.* **9**, 913–921 (2004).
13. T. Dertinger, V. Pacheco, I. von der Hocht, R. Hartmann, I. Gregor, and J. Enderlein, "Two-focus fluorescence correlation spectroscopy: A new tool for accurate and absolute diffusion measurements," *ChemPhysChem.* **8**, 433–443 (2007).
14. D. J. Needleman, Y. Xu, and T. J. Mitchison, "Pin-hole array correlation imaging: Highly parallel fluorescence correlation spectroscopy," *Biophys. J.* **96**, 5050–5059 (2009).
15. N. Dross, C. Spriet, M. Zwerger, G. Müller, W. Waldeck, and J. Langowski, "Mapping EGFP oligomer mobility in living cell nuclei," *PLoS ONE* **4**, e5041 (2009).
16. T. Wilson, R. Juškaitis, M. A. A. Neil, and M. Kozubek, "Confocal microscopy by aperture correlation," *Opt.Lett.* **21**, 1879–1881 (1996).
17. B. Kannan, J. Y. Har, P. Liu, I. Maruyama, J. L. Ding, and T. Wohland, "Electron multiplying charge-coupled device camera based fluorescence correlation spectroscopy," *Anal. chem.* **78**, 3444–3451 (2006).
18. M. Burkhardt and P. Schwille, "Electron multiplying CCD based detection for spatially resolved fluorescence correlation spectroscopy," *Opt. Express* **14**, 5013 (2006).
19. M. K. Landsberg, G. Herbomel, I. Wang, J. Derouard, C. Vourc'h, Y. Usso, C. Souchier, and A. Delon, "Cellular response to heat shock studied by multifocal fluorescence correlation spectroscopy," *Biophys. J.* **103**, 1110–1119 (2012).
20. D. R. Sisan, R. Arevalo, C. Graves, R. McAllister, and J. S. Urbach, "Spatially resolved fluorescence correlation spectroscopy using a spinning disk confocal microscope," *Biophys. J.* **91**, 4241–4252 (2006).
21. P. W. Wiseman, C. M. Brown, D. J. Webb, B. Hebert, N. L. Johnson, J. a. Squier, M. H. Ellisman, and a. F. Horwitz, "Spatial mapping of integrin interactions and dynamics during cell migration by image correlation microscopy," *J. Cell Sci.* **117**, 5521–5534 (2004).
22. B. Hebert, S. Costantino, and P. W. P. Wiseman, "Spatiotemporal image correlation spectroscopy (STICS) theory, verification, and application to protein velocity mapping in living CHO cells," *Biophys. J.* **88**, 3601–3614 (2005).
23. C. M. Brown, B. Hebert, D. L. Kolin, J. Zareno, L. Whitmore, A. R. Horwitz, and P. W. Wiseman, "Probing the integrin-actin linkage using high-resolution protein velocity mapping," *J. Cell Sci.* **119**, 5204–5214 (2006).
24. M. Digman, C. Brown, and P. Sengupta, "Measuring fast dynamics in solutions and cells with a laser scanning microscope," *Biophys. J.* **89** 1317–1327 (2005).
25. S. C. P. Norris, J. Humpolíčková, E. Amler, M. Huranová, M. Buzgo, R. Machán, D. Lukáš, and M. Hof, "Raster image correlation spectroscopy as a novel tool to study interactions of macromolecules with nanofiber scaffolds," *Acta Biomater.* **7**, 4195–4203 (2011).
26. R. A. Colyer, G. Scalia, I. Rech, A. Gulinatti, M. Ghioni, S. Cova, S. Weiss, and X. Michalet, "High-throughput FCS using an LCOS spatial light modulator and an 8 x 1 SPAD array," *Biomed. Opt. Express* **1**, 1408–1431 (2010).
27. R. A. Colyer, G. Scalia, F. a. Villa, F. Guerrieri, S. Tisa, F. Zappa, S. Cova, S. Weiss, and X. Michalet, "Ultra high-throughput single molecule spectroscopy with a 1024 pixel SPAD," in "Proc. SPIE," , vol. 7905 790503–1 (2011).
28. J. R. Unruh and E. Gratton, "Analysis of molecular concentration and brightness from fluorescence fluctuation data with an electron multiplied CCD camera," *Biophys. J.* **95**, 5385–5398 (2008).
29. D. Oh, A. Zidovska, Y. Xu, and D. J. Needleman, "Development of time-integrated multipoint moment analysis

- for spatially resolved fluctuation spectroscopy with high time resolution,” *Biophys. J.* **101**, 1546–1554 (2011).
30. B. Kannan, L. Guo, T. Sudhakaran, S. Ahmed, I. Maruyama, and T. Wohland, “Spatially resolved total internal reflection fluorescence correlation microscopy using an electron multiplying charge-coupled device camera,” *Anal. Chem.* **79**, 4463–4470 (2007).
 31. J. Sankaran, M. Manna, L. Guo, R. Kraut, and T. Wohland, “Diffusion, transport, and cell membrane organization investigated by imaging fluorescence cross-correlation spectroscopy,” *Biophys. J.* **97**, 2630–2639 (2009).
 32. J. Huisken, J. Swoger, F. Del Bene, J. Wittbrodt, E. H. K. Stelzer, and F. D. Bene, “Optical sectioning deep inside live embryos by selective plane illumination microscopy,” *Science* **305**, 1007–1009 (2004).
 33. K. Greger, J. Swoger, and E. H. K. Stelzer, “Basic building units and properties of a fluorescence single plane illumination microscope,” *Rev. Sci. Instrum.* **78**, 023705 (2007).
 34. T. Wohland, X. Shi, J. Sankaran, and E. H. K. Stelzer, “Single plane illumination fluorescence correlation spectroscopy (SPIM-FCS) probes inhomogeneous three-dimensional environments,” *Opt. Express* **18**, 1317–1327 (2010).
 35. J. Capoulade, M. Wachsmuth, L. Hufnagel, and M. Knop, “Quantitative fluorescence imaging of protein diffusion and interaction in living cells,” *Nat. Biotechnol.* **29**, 835–839 (2011).
 36. L. C. Hwang and T. Wohland, “Recent advances in fluorescence cross-correlation spectroscopy,” *Cell Bio-chem. Biophys.* **49**, 1–13 (2007).
 37. E. Baumgart and U. Kubitscheck, “Scanned light sheet microscopy with confocal slit detection,” *Opt. Express* **20**, 21805–21814 (2012).
 38. F. Bestvater, Z. Seghiri, M. S. Kang, N. Gröner, J. Y. Lee, K.-B. Im, and M. Wachsmuth, “EMCCD-based spectrally resolved fluorescence correlation spectroscopy,” *Opt. Express* **18**, 23818–23828 (2010).
 39. J. Sankaran, X. Shi, L. Y. Ho, E. H. K. Stelzer, and T. Wohland, “ImFCS: a software for imaging FCS data analysis and visualization,” *Opt. Express* **18**, 25468–25481 (2010).
 40. J. Buchholz, J. W. Krieger, G. Mocsár, B. Kreith, E. Charbon, G. Vámosi, U. Kebschull, and J. Langowski, “FPGA implementation of a 32x32 autocorrelator array for analysis of fast image series,” *Opt. Express* **20**, 17767 (2012).
 41. C. Jakob, A. Schwarzbacher, B. Hoppe, and R. Peters, “The development of a digital multichannel correlator system for light scattering experiments,” in “IET Irish Signals and Systems Conference (ISSC 2006),” , vol. 2006 (IEEE, 2006), vol. 2006, pp. 99–103.
 42. C. Jakob, a. T. Schwarzbacher, B. Hoppe, and R. Peters, “A FPGA optimised digital real-time multichannel correlator architecture,” in “10th EuroMicro Conference on Digital System Design Architectures, Methods and Tools (DSD 2007),” (IEEE, 2007), pp. 35–42.
 43. G. Mocsár, B. Kreith, J. Buchholz, J. W. Krieger, J. Langowski, and G. Vámosi, “Note: multiplexed multiple-tau auto- and cross-correlators on a single field programmable gate array,” *Rev. Sci. Instrum.* **83**, 046101 (2012).
 44. S. Kalinin, R. Kühnemuth, H. Vardanyan, and C. a. M. Seidel, “Note: A 4 ns hardware photon correlator based on a general-purpose field-programmable gate array development board implemented in a compact setup for fluorescence correlation spectroscopy,” *Rev. Sci. Instrum.* **83**, 096105 (2012).
 45. X. Michalet, O. H. W. Siegmund, J. V. Vallerga, P. Jelinsky, J. E. Millaud, and S. Weiss, “Detectors for single-molecule fluorescence imaging and spectroscopy,” *J. Mod. Optics* **54**, 239–281 (2007).
 46. L. Carrara, C. Niclass, N. Scheidegger, H. Shea, and E. Charbon, “A gamma, x-ray and high energy proton radiation-tolerant CIS for space applications” in “IEEE International Solid-State Circuits Conference - Digest of Technical Papers,” (IEEE, 2009), pp. 40–41.
 47. J. W. Krieger and J. Langowski, “Quickfit 3.0: A data evaluation application for biophysics,” <http://www.dkfz.de/Macromol/quickfit/> (2013).
 48. N. L. Thompson, *Fluorescence correlation spectroscopy* (Springer, 2002), pp. 337–378.
 49. N. Bag, J. Sankaran, A. Paul, R. S. Kraut, and T. Wohland, “Calibration and limits of camera-based fluorescence correlation spectroscopy: a supported lipid bilayer study,” *ChemPhysChem.* **13**, 2784–2794 (2012).
 50. X. Pan, W. Foo, W. Lim, M. H. Y. Fok, P. Liu, H. Yu, I. Maruyama, and T. Wohland, “Multifunctional fluorescence correlation microscope for intracellular and microfluidic measurements,” *Rev. Sci. Instrum.* **78**, 053711 (2007).
 51. M. Wachsmuth, “Fluoreszenzfluktuationsmikroskopie: Entwicklung eines prototyps, theorie und messung der beweglichkeit von biomolekülen im zellkern: Doctoral dissetation,” Ruprecht-Karls-Universität ,Heidelberg. (2001).
 52. P. Kapusta, “Absolute diffusion coefficients: compilation of reference data for FCS calibration,” *Pico-Quant* pp. 0–1 (2010).
 53. Z. Petrášek, P. Schwille, and Z. Petrášek, “Precise measurement of diffusion coefficients using scanning fluorescence correlation spectroscopy,” *Biophys. J.* **94**, 1437–1448 (2008).
 54. P. J. Keller, A. D. Schmidt, A. Santella, K. Khairy, Z. Bao, J. Wittbrodt, and E. H. K. Stelzer, “Fast, high-contrast imaging of animal development with scanned light sheet-based structured-illumination microscopy,” *Nat. Methods* **7**, 637–642 (2010).
 55. D. Blair and E. Dufresne, “The matlab particle tracking code ,” <http://physics.georgetown.edu/matlab/>.
 56. S. M. Hashmi, M. Loewenberg, and E. R. Dufresne, “Spatially extended FCS for visualizing and quantifying

- high-speed multiphase flows in microchannels," *Opt. Express* **15**, 6528–6533 (2007).
57. A. E. Kamholz, B. H. Weigl, B. a. Finlayson, and P. Yager, "Quantitative analysis of molecular interaction in a microfluidic channel: the T-sensor," *Anal. Chem.* **71**, 5340–5347 (1999).
 58. D. Broboana, C. Mihai Balan, T. Wohland, and C. Balan, "Investigations of the unsteady diffusion process in microchannels," *Chem. Eng. Sci.* **66**, 1962–1972 (2011).
 59. H. Y. Gan, Y. C. Lam, N. T. Nguyen, K. C. Tam, and C. Yang, "Efficient mixing of viscoelastic fluids in a microchannel at low Reynolds number," *Microfluid. Nanofluid.* **3**, 101–108 (2006).
 60. H. C. Berg, *Random walks in biology* (Princeton University Press, 1993).
 61. D. Magde, E. L. Elson, and W. W. Webb, "Fluorescence correlation spectroscopy. II. An experimental realization," *Biopolymers* **13**, 29–61 (1974).
 62. S. Ivanchenko and D. C. Lamb, *Fluorescence correlation spectroscopy: Principles and developments* (Springer, 2011), pp. 1–30.
 63. D. Koppel, "Statistical accuracy in fluorescence correlation spectroscopy," *Phys. Rev. A* **10**, 1938–1945 (1974).
 64. P. Kapusta, M. Wahl, A. Benda, M. Hof, and J. Enderlein, "Fluorescence lifetime correlation spectroscopy," *J. Fluoresc.* **17**, 43–48 (2007).
 65. K. Starchev, J. Zhang, and J. Buffle, "Applications of fluorescence correlation spectroscopy – Particle size effect," *J. Colloid Interface Sci.* **203**, 189–196 (1998).
 66. Y. Reibel, M. Jung, M. Bouhifd, B. Cunin, and C. Draman, "CCD or CMOS camera noise characterisation," *Eur. Phys. J-Appl. Phys.* **21**, 75–80 (2002).
 67. T. Dertinger, R. Colyer, G. Iyer, S. Weiss, and J. Enderlein, "Fast, background-free, 3D super-resolution optical fluctuation imaging (SOFI)," *Proc. Natl. Acad. Sci. U.S.A.* **106**, 22287–22292 (2009).
 68. S. Cox, E. Rosten, J. Monypenny, T. Jovanovic-Talisman, D. T. Burnette, J. Lippincott-Schwartz, G. E. Jones, and R. Heintzmann, "Bayesian localization microscopy reveals nanoscale podosome dynamics," *Nat. Methods* **9**, 195–200 (2012).
 69. C. G. Coates, "Back-illuminated electron multiplying technology: the world's most sensitive CCD for ultralow-light microscopy," in "Proceedings of SPIE," vol. 4962 (SPIE, 2003), pp. 319–328.
 70. C. G. Coates, D. J. Denvir, N. G. McHale, K. D. Thornbury, and M. A. Hollywood, "Optimizing low-light microscopy with back-illuminated electron multiplying charge-coupled device: enhanced sensitivity, speed, and resolution," *J. Biomed. Opt.* **9**, 1244–1252 (2004).
 71. S. Iwabuchi, Y. Maruyama, Y. Ohgishi, M. Muramatsu, N. Karasawa, and T. Hirayama, "A back-illuminated high-sensitivity small-pixel color CMOS image sensor with flexible layout of metal wiring," in "IEEE International Solid State Circuits Conference," (IEEE, 2006), pp. 1171–1178.
 72. T. Joy, S. Pyo, S. Park, C. Choi, C. Palsule, H. Han, C. Feng, S. Lee, J. McKee, P. Altice, C. Hong, C. Boemler, J. Hynczek, M. Louie, J. Lee, D. Kim, H. Haddad, and B. Pain, "Development of a production-ready, back-illuminated CMOS image sensor with small pixels," in "IEEE International Electron Devices Meeting," (IEEE, 2007), pp. 1007–1010.
 73. E. Randone, G. Martini, M. Fathi, and S. Donati, "SPAD-array photoresponse is increased by a factor 35 by use of a microlens array concentrator," in "IEEE LEOS Annual Meeting Conference Proceedings," vol. 46 (IEEE, 2009), pp. 324–325.
 74. E. Charbon, and S. Donati, "SPAD sensors come of age," *Optics & Photonics News* **21**, 35–41 (2010).
 75. M. J. Culbertson, J. T. B. Williams, W. W. L. Cheng, D. A. Stults, E. R. Wiebracht, J. J. Kasianowicz, and D. L. Burden "Numerical fluorescence correlation spectroscopy for the analysis of molecular dynamics under nonstandard conditions," *Anal. Chem.* **79**, 4031–4039 (2007).
 76. H. C. Burstyn, and J. V. Sengers, "Time dependence of critical concentration fluctuations in a binary liquid," *Phys. Rev. A* **27**, 1071–1085 (1983).
-

1. Introduction

Fluorescence correlation spectroscopy (FCS) is widely used for measuring protein dynamics in live cells [1–4] and organisms [5–8]. FCS measures the dynamic properties of particles in a small laser focus by analyzing the emitted fluorescence fluctuations with a correlation analysis [9]. Although initially introduced in the 1970s to measure chemical reaction kinetics [9], it was soon realized that it can be used to great effect in biological measurements. FCS was subsequently implemented in confocal microscopes (cf. Fig. 1(B)) combined with single-photon avalanche diodes (SPADs) with high sensitivity and low dark counts [10]. Here, the focal volume is created by a focused laser beam in conjunction with a pinhole, which rejects out-of-focus light. In this configuration FCS measurements are limited to single or few widely separated points [11–15] due to the crosstalk between adjacent foci. The distance between two pinholes must be larger than 10 pinhole diameters [16–19], which precludes imaging FCS, i. e.

the parallel recording of temporal correlation functions at every image point. This problem was circumvented in spinning disk confocal FCS by scanning widely separated pinholes over the sample [20]. However, in this case the detection efficiency is reduced, since each pinhole resides at each point only a fraction of the time, and the scanning process limits the time resolution.

Other approaches have been used to achieve multiplexed and spatio-temporal FCS. The first approach was spatio-temporal image correlation spectroscopy (STICS) [21–23]. At the time of that work, the time resolution was not sufficient to acquire temporal FCS functions at each spot, but it was used to observe the temporal development of spatial correlations. Raster image correlation spectroscopy (RICS) uses the temporal information inherent in a scanning confocal microscope to allow the calculation of spatio-temporal correlations [24] and can be used to derive diffusion and binding kinetics [25]. However, measurements are still not simultaneous over the whole sample and require laser scanning, which illuminates the whole sample and thus is more prone to bleaching and photodamage.

Multi-spot FCS approaches range from using stopped spinning disks [14] to spatial light modulators [19, 26, 27]. However, all of these approaches allow the measurement of only a limited number of widely separated spots, and thus cannot provide a contiguous image of a sample. An interesting new variant of imaging fluctuation spectroscopy is time-integrated multipoint moment analysis (TIMMA) a generalization of the number and brightness analysis pioneered by Unruh and Gratton [28]. TIMMA decouples the time resolution from the read-out speed of the camera and is instead dependent on the smallest exposure time which is typically much faster than the read-out speed [29].

For true imaging FCS the imaging system has to be fast and suppress out-of-focus light. The latter can be achieved by restricting the illumination profile to a plane orthogonal to the optical axis of the detection system within. Total internal reflection fluorescence (TIRF) provides a ~ 100 nm thin illuminated plane close to a cover slip and with fast and sensitive cameras imaging TIR-FCS was demonstrated [30, 31]. To overcome the restriction of imaging total internal reflection FCS (ITIR-FCS) to 2D samples, selective plane illumination microscopy (SPIM) [32, 33] (cf. Fig. 1(A)) was combined with FCS to allow measurements inside 3D samples, e. g., cells or small embryos [34, 35]. SPIM uses a micrometer-thin light sheet to excite fluorescence in a defined z -section. The detection is performed orthogonal to the illumination. Since only the regions to be measured are illuminated, TIRF microscopy and SPIM limit bleaching and photodamage. This allows to perform more measurements per sample, than in e. g., confocal microscopy based FCS.

In both illumination modes, fast and sensitive cameras are necessary for FCS. In earlier STICS studies [22, 36], mostly the temporal evolution of image correlation functions was observed. Today's cameras are fast enough to also capture the temporal autocorrelation generated by medium-sized and small fluorescent particles in each pixel. Even higher read-out speeds may be achieved by limiting the measurement to single points or single lines on an electron-multiplying charge coupled device (EMCCD) camera. By continuous rolling read-out modes [37], which are limited only by the line shift speed, analog to digital conversion speed and electronics bandwidths, line-read-out times as low as $\sim 30 \mu\text{s}$ were achieved [18, 38].

These new imaging FCS approaches require new ways of recording and treating data. The parallel measurement of thousands to millions of correlation functions needs appropriate data processing. In a typical SPIM-FCS experiment with read-out rates on the order of 10,000 frames per second for $\sim 1,000$ pixels, data can be directly streamed to disk and software correlators can calculate spatial and temporal correlation functions almost in real time [39]. However, with increasing read-out rates this approach is limited and several reports have described the use of field programmable gate arrays (FPGA) to calculate all correlations in real time [40–42]. Recently similar approaches have also been proposed for multi-parameter

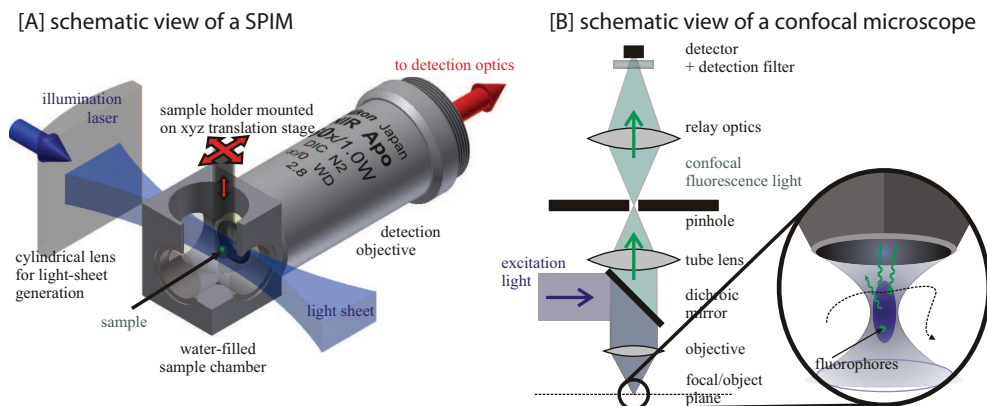


Fig. 1. Schematic Sketches of [A] a selective plane illumination and [B] a confocal microscope.

FCS [43,44]. With the use of these hardware approaches, correlation functions may now be calculated at read-out rates of 100,000 frames per second or more in real time.

In earlier work we have given the analytical expression for SPIM-FCS in the case of diffusion and flow [34]. Here we extend the theory and provide an expression for the effective SPIM detection volume. We then compare four different array detectors, including commercially available EMCCD, sCMOS and CMOS devices as well as a SPAD array. We show that by exploiting the known pixel size of the detectors, the PSF can be determined directly from FCS measurements without using a reference sample of known diffusion coefficient. This way absolute diffusion coefficients can be measured. Finally we will discuss concentration measurements with the array detectors and compare the different devices. A complementary study comparing several image detectors for single-molecule detection was recently published by X. Michalet et al. [45].

2. Materials and methods

Details, including schematic sketches, of the different setups are given in the *supplementary information*. We describe here the systems only briefly.

2.1. SPIM microscopes

Measurements were done on two SPIMs situated in Singapore (SPIM-1) and Heidelberg (SPIM-2). Both are of the type as described in [33]. Both setups use a 60 \times /NA 1.0 detection objective and project the image onto different camera types using the tube lens from the objective manufacturer. In SPIM-1 we mounted one out of four available cameras (*iXon X3 860*, Andor Technology, Belfast, UK; *Evolve 512*, Photometrics, Tucson, United States; *ORCA-Flash4.0* sCMOS Camera, Hamamatsu, Hamamatsu City, Japan and *SA-05* CMOS, Dynamic Analysis System Pte Ltd, Singapore). In SPIM-2 an Andor *iXon X3 860* or a *pco.edge* sCMOS (PCO AG, Kehlheim, Germany) is mounted together with a *Radhard2* SPAD array [46]. The SPAD array uses a tube lens of half the usual focal length to increase the fluorescence intensity on the sensor. This decreases the magnification, but conserves the numerical aperture of the detection objective. The light is split between both image sensors using a 50:50 beam splitter plate. The light sheets are projected with NA 0.25 (SPIM-1) or NA 0.3 (SPIM-2) air objectives through a No. 1 cover slip into a custom-built and water filled sample chamber, sealed against the detection objective. In both cases the back-aperture is overfilled with illumination light and the resulting light sheets differ only slightly in width

($1/e^2$ -half widths: $(1.42 \pm 0.05) \mu\text{m}$ in SPIM-1 and $(1.2 \pm 0.20) \mu\text{m}$ in SPIM-2). The sample is mounted on a motorized XYZ-stage that allows easy and automated translation.

The cameras yield an intensity time trace $I(t)$ for every pixel. Then the autocorrelation function

$$G(\tau) = \frac{\langle I(t) \cdot I(t + \tau) \rangle}{\langle I(t) \rangle^2} \quad (1)$$

is calculated in software. Here $\langle \cdot \rangle$ denote time averaging. Finally a least-squares fit is performed, using the following model function [34, 39]:

$$G(\tau) = \frac{1}{\sqrt{\pi} \cdot w_z a^2 C} \left(\frac{\sqrt{4D\tau + w_{xy}^2}}{\sqrt{\pi} \cdot a} \cdot \left(e^{-\left(\frac{a^2}{4D\tau + w_{xy}^2}\right)} - 1 \right) + \text{erf} \left(\frac{a}{\sqrt{4D\tau + w_{xy}^2}} \right) \right)^2 \cdot \left(1 + \frac{4D\tau}{w_z^2} \right)^{-1/2} + G_\infty \quad (2)$$

where C is the average concentration of particles in the observation volume V_{eff} from which the average particle number N is $C = N/V_{\text{eff}}$. The particular V_{eff} for SPIM-FCS is given in Eq. (5) and will be discussed below in section 2.2. The parameter a is the side length of a square pixel in object space, D is the diffusion coefficient, and w_{xy} and w_z are the $1/e^2$ radii of the PSF in the xy and the z -plane. G_∞ is the convergence value for long correlation times, which is expected to be 1 for the definition of $G(\tau)$ in Eq. (1).

For the *Radhard2* SPAD array, data was fitted with a standard Gaussian FCS model Eq. (6) instead of the camera model Eq. (2). We chose this model because the array consists of 32×32 circular SPADs with $4 \mu\text{m}$ diameter of the active area and a grid spacing of $30 \mu\text{m}$ in both directions (i. e. 133 nm diameter and $1 \mu\text{m}$ spacing in the object plane). Due to the round shape and the small size, a rotationally symmetric Gaussian focal volume is a good approximation (for details on the sensor and its detection volume, see also the *supplementary information* and Refs. [40,46]). Fits were performed in one of our imaging FCS evaluation packages ImFCS [39] or QuickFit 3.0 [47].

2.2. Determination of the observation volume

The molecule detection efficiency (MDE) in FCS describes the measurement volume [10, 48]:

$$\text{MDE}(\vec{x}) = \text{CEF}(\vec{x}) \cdot I_{\text{ill}}(\vec{x}), \quad (3)$$

where \vec{x} is position in object space, $\text{CEF}(\vec{x})$ is the collection efficiency function which determines the amount of light from the sample registered by a detector element in the optical system and $I_{\text{ill}}(\vec{x})$ is the light intensity distribution of the excitation source, in our case the light sheet. The CEF is the convolution of the pinhole, in our case the (binned) pixels on the camera, with the PSF of the optical system. In previous publications we have already derived the xy -extension of the CEF for pixels with sufficient size to detect the full light sheet thickness [31, 39] and have provided a method to determine the PSF experimentally [49]. Here we extend this to the case of light sheet illumination and pixel detection of any size, even for pixel sizes which are small and lead to spatial filtering of the light sheet.

In the z -direction the light sheet has an approximately Gaussian profile with $1/e^2$ -width w_{ill} . The CEF can also be approximated as a Gaussian function with $1/e^2$ -width w_{det} . Then the overall width w_z of the MDE can be calculated as:

$$\frac{1}{w_z^2} = \frac{1}{w_{\text{ill}}^2} + \frac{1}{w_{\text{det}}^2} \quad (4)$$

So the width of the MDE is either limited by the depth of focus of the pinhole CEF or by the width of the light sheet profile. With this definition, the effective detection volume of a SPIM pixel can be expressed as:

$$V_{\text{eff}} := \frac{(\int \text{MDE}(\vec{x}) \, dV)^2}{\int \text{MDE}^2(\vec{x}) \, dV} = \frac{\sqrt{\pi} \cdot a^2 w_z}{\left(\text{erf}\left(\frac{a}{w_{xy}}\right) + \frac{w_{xy}}{\sqrt{\pi} \cdot a} \left(e^{-(a/w_{xy})^2} - 1 \right) \right)^2} \quad (5)$$

This definition differs from the one used in our earlier publication [34]. It allows to compare directly the focal volume of camera-based and confocal FCS. Note that this expression can be derived from Eq. (2) by requiring that $G(0) = G_\infty + 1/N$.

An important advantage of spatio-temporal correlation methods on SPIM and TIRF microscopes is that they require few calibrations over time. Confocal FCS methods need a calibration of the microscope parameters before and after the measurements, to ensure that the observation volume has not changed. De-alignment between laser and pinhole or changes in the laser beam profile can happen due to temperature changes or drift within the optical system.

SPIM and TIRF microscopes overcome this problem by illuminating a large field of view with an approximately homogeneous intensity, so the exact lateral position of the pixels is non-critical. Second, the shape of the observation volume does not significantly depend on the alignment and is mostly defined by the quality of the detection objective, which does not typically vary over its lifetime. Third, array detectors introduce a ruler into the system, as the distance between pixels is known accurately (the sensor dimensions are known with nanometer precision and the magnification can be determined easily). This allows to determine the PSF without having to rely on a calibration sample of known diffusion coefficient.

The calibration method described in [49] for a TIRF microscope can be extended to a SPIM: The longitudinal width w_z can either be measured by bead scans or is calculated from Eq. (4). Then the diffusion coefficient D can be measured independently of the PSF width w_{xy} if a large pixel binning (i. e. $a \gg w_{xy}$) is used. Finally w_{xy} can be determined by a fit without binning and a known D irrespective of pixel size a . A detailed protocol is given in the *supplementary information*. For the SPAD array a different method was used, which is based on pixel-pixel crosscorrelations and is also elaborated in the *supplementary information*. Typically the calibration of SPIM and TIRF microscopes is stable over a year or more in our labs, cf. [49]. In SPIM the only variable is the width of the light sheet, which can routinely be checked. The calibrated size of the PSF (cf. Tab. 1) in the SPIM setups was confirmed by bead scans (see *supplementary information*).

2.3. Confocal FCS measurements

Confocal measurements were performed on customized instruments in both laboratories (Confocal-1 in Singapore and Confocal-2 in Heidelberg) [50, 51]. Detailed descriptions are provided in the *supplementary information*. In brief, both instruments were based on inverted microscopes (Olympus IX 70/71). Fluorescence was excited with a 488-nm laser line, which was focused by a water-immersion objective (60 \times , NA 1.2; Olympus, Tokyo, Japan) into the sample. The laser power was set to 12 – 30 W/cm² above the objective. The fluorescence light emitted from the sample was collected by the same objective, was filtered spectrally by a band-pass filter and spatially by a pinhole. The light from the pinhole was imaged onto an avalanche photodiode, which operated in photon counting mode. The autocorrelation curves were computed online by a hardware correlator. Data evaluation was performed on self-written programs in IGOR Pro 6.2 (Wavemetrics, Lake Oswego, OR, USA) or QuickFit 3.0 [47] with

a simple one-component fit model:

$$g(\tau) = G_{\infty} + \frac{1}{N} \cdot \left(1 + \frac{4D \cdot \tau}{w_{xy}^2}\right)^{-1} \cdot \left(1 + \frac{4D \cdot \tau}{K^2 \cdot w_{xy}^2}\right)^{-1/2} \quad (6)$$

where G_{∞} is the convergence value for long correlation times, N is the number of particles in the focal volume, D is the diffusion coefficient of the particles and $K = w_z/w_{xy}$ is the axial ratio of the Gaussian focal volume. The lateral focal $1/e^2$ -half width w_{xy} was calibrated using a 10 nM Atto-488 solution on Confocal-1 ($D_{20^{\circ}\text{C}} = (350 \pm 6) \mu\text{m}^2/\text{s}$ [52]) and a 20 nM Alexa-488 solution on Confocal-2 ($D_{20^{\circ}\text{C}} = 407 \mu\text{m}^2/\text{s}$ [53]). The axial ratio K was fixed to 5 or 8, depending on the microscope. The overall particle concentration in the sample can be calculated using the effective focal volume $V_{\text{eff}}^{(\text{confocal})}$ for the confocal case as:

$$c = \frac{N}{V_{\text{eff}}^{(\text{confocal})}} = \frac{N}{\pi^{3/2} \cdot w_{xy}^3 \cdot K} \quad (7)$$

2.4. Sample preparation

Carboxylate-modified microspheres (0.1 μm and 0.2 μm , yellow-green fluorescent beads 505/515, 2.0% solids, Invitrogen, Singapore) were diluted in deionized water (DI) or a slightly alkaline buffer (10 mM Tris-HCl, pH 8.5) to the desired working concentration (0.1-1.1 nM). The diluted solution was sonicated for 15-30 minutes in a bath sonicator (FB15051 Model, Fisher Scientific, Singapore) to disperse aggregates. The samples (typically 20-50 μl) were mounted in transparent (UV-VIS-IR transparency: 90%), heat sealed plastic bags (fluorinated polyethylene propylene films, thickness 13.0 μm , refractive index 1.341 – 1.347, Katco Ltd., United Kingdom, or Lumox Folie 25 M, thickness 25 μm , Sarstedt AG & Co, Nümbrecht, Germany). Measurements in different laboratories were performed at different temperatures (20°C or 25°C). For comparison all diffusion coefficients were recalculated to their value at 20°C.

2.5. Microchannel fabrication

Silicone curing agent and prepolymer polydimethylsiloxane (PDMS, Sylgard 184, Dow Corning, Singapore) were mixed in a 1:10 ratio by weight. The mixture was degassed and then poured into a master mold ($A = 300 \times 380 \mu\text{m}^2$) with two inlets and one outlet. Overnight heating at 65°C in an oven cured the PDMS gel to hardened PDMS, which was peeled off from the master mold. The PDMS channel was treated in an oxygen plasma cleaner (PDC-32 G, Harrick) for one minute after which it was bonded to a glass cover slide ($24 \times 75 \text{ mm}^2$, No-1, Fisher Scientific, Singapore). Sample mounting is described in the *supplementary information*.

3. Results and discussion

3.1. Light sheet characterization

The area over which SPIM-FCS can provide accurate and consistent correlation functions depends on the properties and quality of the light sheet, which is determined mostly by the optical quality of the beam forming components (cylindrical lens and low NA projection objective). The height of the light sheet can be adjusted by apertures in the setup. While light sheets of better quality can be created by a digital scanned laser light sheet microscope (DSLIM) [54], this scanning process interferes with the recording of correlation functions at similar or faster time scales as the scanning process. In addition, each point is illuminated only part of the time of every scan. This reduces the signal strength, rendering an unscanned light sheet the better illumination alternative.

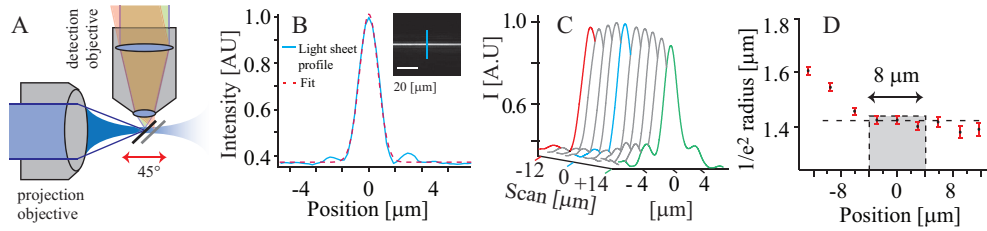


Fig. 2. Exemplary light sheet characterization of SPIM1: [A] illustrates the scanning of a 45° mirror to image the light sheet. [B] The intensity profile of the light sheet (blue line) at the central region of the field of view and a Gaussian fit to the profile (red dashed line). [C] The light sheet intensity profile at different regions of the camera along the illumination direction. [D] Thickness variation (obtained from the Gaussian fit) along the illumination axis. The grey box marks the central region ($\sim 8 \mu\text{m}$ wide) with approximately constant light sheet thickness.

For the measurement of absolute diffusion coefficients the extension of the light sheet has to be known and the contribution of the side lobes of the light sheet have to be minimized [34]. Therefore, we record the light sheet extension before measurements and use only that part of the light sheet, which shows a consistent width and low side lobes. The light sheet is visualized by a mirror aligned at 45° to the optical axis of the illumination objective (see Fig. 2(A)). The mirror can be scanned using the motorized sample holder. In Fig. 2 we show light sheet cross sections of SPIM-1 at different positions over a range of $26 \mu\text{m}$ along this axis. The $1/e^2$ radius in the center of the light sheet is $(1.42 \pm 0.05) \mu\text{m}$ with side lobe contribution of 8-10% (area under the curve). In our measurements we use the central $8 \mu\text{m}$ (shown as a grey box Fig. 2D) of the light sheet over which the $1/e^2$ radius does not vary significantly and the side lobes are small. The second SPIM setup showed slightly different light sheet characteristics. It was typically $(1.2 \pm 0.2) \mu\text{m}$ thick in the central $8 \mu\text{m}$ of the field of view. At the chosen magnification of 60x this corresponds to 20 pixels for the *iXon X3 860*, 24 pixels for the *SA-05 CMOS*, 30 pixels for the *Evolve 512* and 74 pixels for the *ORCA-Flash4.0* and the *pco.edge*. From the SPAD array 8 pixels were used due to the lower magnification of 30x.

3.2. Array detectors

Here we evaluate the FCS performance of various array detectors with different effective pixel sizes, quantum efficiencies, and read-out speeds, by measuring the diffusion coefficient of $0.1 \mu\text{m}$ diameter fluorescent microspheres. For each camera a subregion of the sensor was chosen that is not larger than the area of approximately constant light sheet thickness (region of interest, ROI). Then the fastest possible read-out speed for this region was selected. For comparison the same sample was measured on a confocal microscope. Table 1 summarizes the results for the different cameras and the camera specifications. Example correlation curves of all sensors are shown in Fig. 3. As can be seen, the theoretical diffusion coefficient at 20°C for $0.1 \mu\text{m}$ beads in water $D^{(\text{theo})} = 4.29 \mu\text{m}^2/\text{s}$ can be determined within the margins of error by all cameras.

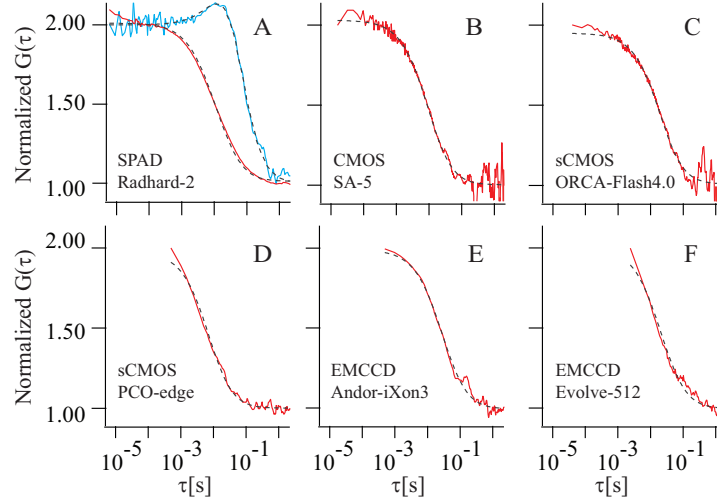


Fig. 3. Exemplary normalized ACFs (red), 2f-FCCS (blue) plots and fit results (black dashed) for $0.1 \mu\text{m}$ diameter fluorescent microspheres at fastest read-out speed: [A] SPAD array detector with minimal lag time $\tau_{\min} = 3 \mu\text{s}$, [B] SA-05 CMOS $\tau_{\min} = 16.6 \mu\text{s}$, [C] ORCA-Flash4.0 sCMOS: $\tau_{\min} = 38.9 \mu\text{s}$, [D] pco.edge sCMOS: $\tau_{\min} = 495 \mu\text{s}$, [E] Andor iXon X3 860 EMCCD: $\tau_{\min} = 495 \mu\text{s}$ and [F] Evolve 512 EMCCD: $\tau_{\min} = 2380 \mu\text{s}$. All curves are normalized for the zero-lag amplitude obtained from the fits.

3.3. Absolute diffusion coefficients

The determination of absolute diffusion coefficients was tested by measuring the diffusion coefficients of fluorescent polystyrene beads of $0.2 \mu\text{m}$ diameter in aqueous solution (theoretical value $D_{20^\circ\text{C}}^{(\text{theo})} = (2.04 \pm 0.1) \mu\text{m}^2/\text{s}$, errors estimated from the given size distribution of the beads) with SPIM-FCS and three other, but independent methods. The iXon X3 860 EMCCD has been used for SPIM based measurements in this section. The results are summarized in Tab. 2 and Fig. 4. For the SPIM-FCS measurement we obtained $D = (1.91 \pm 0.7) \mu\text{m}^2/\text{s}$. FCS measurements in a standard confocal microscope (Confocal-1, see section 2.3 and *supplementary information*) gave $D = (2.10 \pm 0.05) \mu\text{m}^2/\text{s}$. A single particle tracking (SPT) analysis with a Matlab based particle tracking code [55] gave $D = (2.05 \pm 0.11) \mu\text{m}^2/\text{s}$ (see Fig. 4(C)). Lastly, we exploited the diffusion-driven concentration gradient profile in a Y-shaped micro-channel [56–58] with a cross-section of $H \times W = 300 \times 380 \mu\text{m}^2$ (see Fig. 4(D-E) and *supplementary information*). A solution with fluorescent beads is introduced into one inlet while the pure buffer is introduced into the other. Due to laminar flow in our experimental conditions (Reynolds number $\text{Re} < 1$) [59], mixing between the two adjacent streams happens only by diffusion. With increasing length of the channel the streams have more time to interact and one can observe the development of a concentration profile at the interface between the streams over time. By fitting this concentration profile to its analytic solution [57, 60] one can determine the diffusion coefficient D , if the exact time t over which diffusion took place is known. In the micro-channel this time t is given by the flow speed of the solution v and the distance d of the measurement position from the first contact of the two buffer streams ($d = t \cdot v$). The analytic solution for one-dimensional diffusion across a plane with concentration $c(x > x_0) = c_0$ at one side and concentration $c(x \leq x_0) = 0$ on the other side is given by:

$$c(x) = b + c_0 \cdot \text{erf}\left(\frac{x - x_0}{\sqrt{4Dt}}\right) \quad (8)$$

Table 1. Summary of the results obtained with all types of array detectors for a sample of $0.1 \mu\text{m}$ fluorescent latex beads in water. All diffusion coefficients are renormalized to 20°C and average \pm standard deviation over the specified number of pixels are given. The table also contains the camera specifications (as provided by the manufacturers) and focus parameters.

	<i>Radhard2</i>	<i>SA-05</i>	<i>ORCA-Flash4.0</i>	<i>pco.edge</i>	<i>iXon X3 860</i>	<i>Evolve 512</i>	<i>confocal FCS</i>
technology	SPAD array	CMOS	sCMOS	sCMOS	EMCCD	EMCCD	SPAD
quantum efficiency[†] @ 525 nm	35%	35%	70%	54%	95%	95%	55%
pixel size [μm]	4	20	6.5	6.5	24	16	—
pixel pitch [μm]	30	20	6.5	6.5	24	16	—
exposure time [μs]		16.6	38.80	486	450	2000	—
cycle time [μs]	3	16.8	38.95	495	489	2380	—
lat. size w_{xy} [nm]	523 ± 59	620 ± 62.8	445 ± 32.5	382 ± 64	620 ± 200	574 ± 61.4	232 ± 4
long. size w_z [nm]	857 ± 95	1395 ± 45	850 ± 58	810 ± 230	1115 ± 100	1370 ± 37	1856 ± 32
obs. volume V_{eff} [fl]	1.31	3.28	0.96	0.67	2.72	2.69	0.56
acquired frames	6,291,456	165,400	85,000	50,000	60,000	20,000	—
ROI [pixels]	8×12	20×20	6×100	32×32	20×20	20×20	6 runs
measured D [$\mu\text{m}^2/\text{s}$]	4.23 ± 0.46	4.43 ± 1.92	4.16 ± 1.84	4.93 ± 1.69	4.20 ± 1.10	3.84 ± 0.78	4.10 ± 0.05

[†] Technically in SPADs the quantum efficiency (QE) is slightly higher than indicated and the probability of a photoelectron triggering an avalanche is < 1 . However, for simplicity, we prefer to equate QE to the photon detection probability (PDP) in this paper.

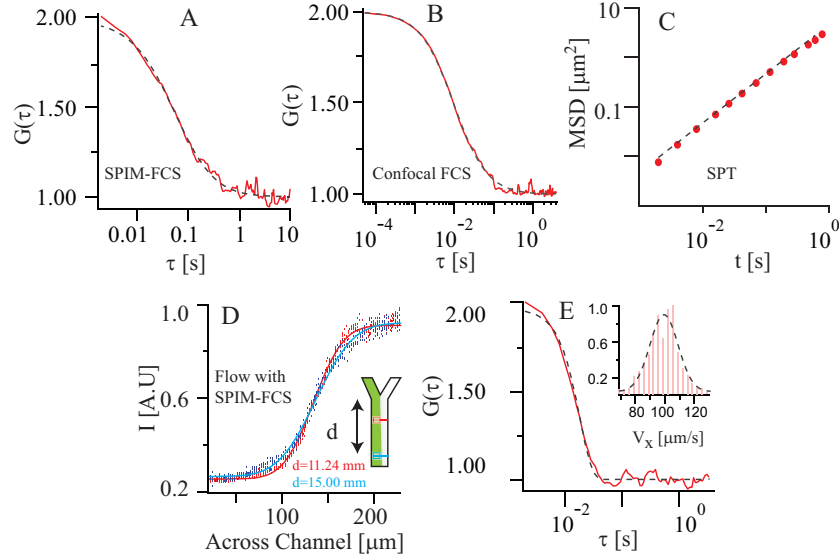


Fig. 4. Absolute diffusion coefficient determination for $0.2 \mu\text{m}$ diameter fluorescent microspheres by four different methods. Each subplot shows measured data (red, blue) and a fit to the data (dashed lines). [A] exemplary SPIM-FCS measurement, [B] Confocal FCS Measurement, [C] Mean-squared displacement curve (MSD) from a single particle tracking experiment, [D] intensity profile across the microchannel at two positions, [E] exemplary SPIM-FCS fit and velocity distribution used to determine the flow speed for [D].

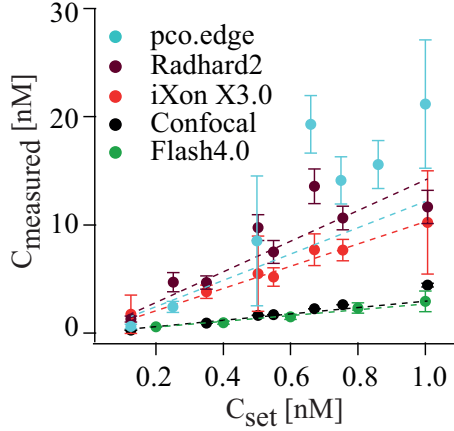
Here b is an offset value, and c_0 , x_0 and D are fitting parameters. The solutions were injected into the microchannel using syringe pumps. As the flow speed created by these pumps is not known precisely, we determined it by SPIM-FCS measurements using a model that also incorporates the flow speed (for the fit model, see Ref. [39]), which yielded $v = (100 \pm 21.2) \mu\text{m/s}$ (see Fig. 4(E)). We then used the intensity profile in the center of the channel, to avoid wall effects, and fitted the profile to Eq. (8) to determine D . Measurements at two positions ($d_1 = 11 \text{ mm}$ and $d_2 = 15 \text{ mm}$) yielded $D(d_1) = (2.20 \pm 0.25) \mu\text{m}^2/\text{s}$ and $D(d_2) = (2.40 \pm 0.20) \mu\text{m}^2/\text{s}$. All determinations of the diffusion coefficients agreed within the margins of error (cf. Tab. 2), confirming the capability of SPIM-FCS to determine absolute diffusion coefficients.

Table 2. Diffusion coefficient D of $0.2 \mu\text{m}$ microsphere determined with SPIM-FCS, Confocal FCS, single particle tracking (SPIM-SPT) and measuring the lateral diffusive mixing in a Y-shaped microchannel (“SPIM-Flow”).

	SPIM-FCS	Confocal FCS	SPIM-SPT	SPIM-Flow
$D[\mu\text{m}^2/\text{s}]$	1.9 ± 0.70	2.10 ± 0.05	2.05 ± 0.11	$2.2 \pm 0.25, 2.4 \pm 0.20$

3.4. Concentrations

Concentration measurements in FCS rely on the fact that the autocorrelation function at a lag time of 0 s represents the variance of the photon counts determined by the number of particles in the observation volume, which follow a Poisson distribution with the variance being equal to



Fit results:

sensor	slope α
<i>Radhard2</i>	14.15
<i>pco.edge</i>	12.19
<i>iXon X3 860</i>	10.31
<i>confocal FCS</i>	2.94
<i>ORCA-Flash4.0</i>	2.73

Fig. 5. Results of a dilution series measurement of $0.1 \mu\text{m}$ diameter fluorescent microspheres in water. The plot shows the expected value C_{set} plotted against the measured value C_{measured} (circles) and linear fits to these (dashed lines, intercept at $C_{\text{set}} = C_{\text{measured}} = 0$). Data was acquired on different setups: A confocal microscope (black), and on a SPIM with four different detectors (green: *ORCA-Flash4.0*, red: *iXon X3 860*, brown: *Radhard2*, blue: *pco.edge*). datapoints are average \pm standard deviation as in Tab. 1. The fitting has been weighted with standard deviation.

the mean [61]. The amplitude of the ACF is thus given by:

$$G(0) - G_{\infty} = \frac{\langle \delta I^2(t) \rangle}{\langle I(t) \rangle^2} = \frac{N}{N^2} = \frac{1}{N} = \frac{V_{\text{eff}}}{C}, \quad (9)$$

where N is the average particle number in the observation volume V_{eff} , $C = N/V_{\text{eff}}$ is the average concentration and the background-corrected intensity $I(t) = \langle I(t) \rangle + \delta I(t)$ is split into a constant offset $\langle I(t) \rangle$ and the fluctuations $\delta I(t)$ with $\langle \delta I(t) \rangle = 0$. When the observation volume is known one can then calculate absolute concentrations from FCS measurements [62]. In our measurements we could only get a linear relation

$$C_{\text{measured}}(C_{\text{set}}) = C_0 + \alpha \cdot C_{\text{set}} \quad (10)$$

between the set concentration C_{set} and measured concentration C_{measured} . The results of such a dilution series of $0.1 \mu\text{m}$ fluorescent microspheres with different image sensors is shown in Fig. 5. The intercept $C_0 = 0 \text{ nM}$ was still obtained with all tested cameras, as it mostly depends on the background signal and camera offset that were corrected before the fit [63]. But the slope α differed for all measurements and was also different from the expected value $\alpha = 1$. Several factors might lead to this overestimation of the concentration: In the confocal case it is well known that after pulsing of the SPADs constitutes a background that cannot be easily removed and will lead to an increase in apparent particle number of a factor 2 – 3 as seen here, but which can be corrected by fluorescence lifetime correlation spectroscopy (FLCS) [64]. Similarly, Oh et al. demonstrated that for an EMCCD the noise can be corrected by splitting the image on two halves of the detector and then cross-correlating corresponding pixels which detect the same volume [29]. This correction is similar to the one used to correct for afterpulsing of APDs in confocal FCS [76]. A further factor of 1.2 – 1.3 stems from the non-vanishing size of the beads in relation to the focus size, as the used models assume point-like fluorophores [65]. Another problem is that Eq. (2) is valid for a 3D Gaussian PSF and is therefore only an approximation of the real PSF. Bead scans show that the lateral PSF size w_{xy} is not independent of the position z

on the optical axis (an assumption for Eq. (2)) and that low-intensity sidelobes are sometimes visible (see *supplementary information*). We performed simulations on these effects (also see *supplementary information*) and found an expected overestimation of the concentration by not more than a factor 1.4 – 1.5. It should be noted that the simulations show that despite the influence of the side lobes on the concentrations the measured diffusion coefficient does not change and is recovered accurately. Eq. (2) could be replaced by a model taking at least the z -dependence of w_{xy} into account, but at the cost of having to solve numerical integrals in every evaluation [13, 75]. A third factor influencing the measured particle number is a biasing of the fits, if the plateau of the correlation function is not captured due to the low framerate of the sensors. This effect can be seen in Fig. 3(C-F), where the fits (dashed lines) are systematically below the data (red line) for small lag times.

We think the remaining overestimation by a factor of $\sim 2 - 5$ can only be explained by detector artifacts: For the photon counting *Radhard2* the overestimation might be explained by a certain clipping of the correlation functions (i. e. an artificially lower correlation amplitude and thus higher particle number) due to the fact that per read-out cycle only 0 or 1 photons can be counted. If two or more photons are detected by the SPAD, they are still counted as 1 photon only. In addition, all the cameras used in this paper are analog detectors and their grey values $I(t)$ do not follow a Poisson distribution (as the photon counting SPADs do), where mean equals variance [66]. Nevertheless all fit models in this paper assume a Poisson photon counting statistics and therefore we can not expect to measure the absolute concentration with the cameras used here. This fact has already been reported by Unruh and Gratton for the Number & Brightness analysis [28] and was also described recently by Kloster-Landsberg et al. [19]. Similar to these publications, we still see a linear dependence between the measured and set concentration. So a definite answer to the question of why the concentration is overestimated in camera-based FCS will require a much deeper analysis of the detectors, which is out of scope for this paper. Therefore relative concentration measurements are possible in camera FCS and especially imaging FCS. An absolute measurement is possible if one possesses a standardized calibration solution.

4. Camera comparison

At the time of writing, the most suitable array detectors for SPIM-FCS are EMCCD cameras with their high quantum efficiencies ($>90\%$), fill factors of nearly 100% and reduction of read-out noise by on chip amplification. They reach frame rates of $\sim 3,000$ fps for reasonable subregions of around 10 lines and approx 20 pixels each. Frame rates of up to 70,000 fps are possible when only a single line is used [18, 38], but this sacrifices the imaging capability and is thus not a viable alternative for SPIM-FCS. The physical size of the pixels is well adapted to the typical magnification (60-100 \times) and numerical apertures (NA 0.8-1.2) used in SPIM-FCS and corresponds to about half the size of the PSF. This is a good compromise between light collection efficiency and spatial resolution for SPIM-FCS. The size of the detection volume obtained with the EMCCD pixels and our NA 1.0 objectives (cf. Tab. 1) is well suited for the 1.2 – 1.4 μm thick light sheets used in our setups. This lateral and longitudinal resolution is also well suited for measurements in single cells. However, EMCCDs have also distinct disadvantages. Their read-out speed is limited to a couple of thousand frames per second and thus is just a bit too slow to capture freely diffusing small molecules in solution. It is also at the limit of detecting free fluorescent proteins in the cytoplasm of cells.

On the other hand, sCMOS cameras already provide read-out speeds of more than 25,000 fps ($< 40 \mu\text{s}$ per frame) which is fast enough to capture also the fast dynamics of fluorescent proteins in cells (correlation decay times on the order of 100 μs and less). The high frame rates of sCMOS cameras can be sustained over many more pixels compared to EMCCDs. The

smaller pixel size of the sCMOS cameras (typically $\sim 3.5 - 6.5 \mu\text{m}$) leads to a stronger pinhole effect and thus longitudinally and also laterally to a smaller detection volume. These cameras oversample the PSF by 5–15 times but also collect fewer photons for each pixel. The latter effect can be circumvented by pixel binning and thus opens the possibility to perform FCS, with larger and binned pixels, with super-resolution techniques such as super-resolution optical fluctuation imaging (SOFI) [67] and single-molecule localization microscopy [68]. Active-pixel sensors (like CMOS cameras and SPAD arrays) are pixel-addressable, so each pixel can be read individually and no shifting is necessary. This makes them more versatile than passive-pixel sensors (like EMCCDs), as e. g., the frame rate of subregions does not depend on the position of the subregion. Because there is no need for a shift operation, no additional noise is created.

Even faster read-out speeds can be achieved routinely with SPAD arrays, which can reach between 300,000 fps (for a 32×32 pixel frame) and 2,400,000 fps (for a 4×32 pixel ROI), at present and thus are truly fast enough to capture also small fluorescent molecules (e. g., free dyes) diffusing in solution. In addition, SPAD arrays are true single-photon counting devices and online-data processing hardware for SPIM-FCS has already been designed and tested [40]. The disadvantages of SPAD arrays at the time of writing are their lower quantum efficiency ($\sim 35\%$) as compared to EMCCDs, overall smaller number of pixels, especially when compared to sCMOS cameras, and their small fill factor ($\sim 2-4\%$) which compromises the collection efficiency of the device. This can be addressed in the future by back-illuminated sensors and microlens arrays [69–73]. Also larger SPADs and thus a larger sensitive area per pixel become possible with newer microchip production processes that reduce the size of the electronics in each pixel, leaving more room for the SPAD [27, 74]. These developments could give SPAD arrays the edge over other devices.

5. Conclusion

In this work we tested several array detectors for their suitability for imaging FCS. SPAD arrays perform fastest ($\sim 300,000$ fps) and have the best precision (standard deviation $\sim 10\%$) for diffusion coefficient measurements. They would be ideal detectors since they can operate in photon counting mode, but their restricted sensitivity (quantum efficiency: $\sim 35\%$) and fill factor ($\sim 2-4\%$) still limits their usability. The second fastest detectors are sCMOS cameras have high frame rates of at least ($\sim 25,000$ fps). They have a higher quantum efficiency ($\sim 50-70\%$) than SPAD arrays but they can also reach frame rates in the microsecond range, similar to SPADs in the microsecond range. The CMOS used here has similar properties to the sCMOS with high frame rates of at least ($50,000$ fps) but lower QE ($\sim 35\%$) and similar precision. However, they show the worst precision (standard deviation $\sim 30\%$) in this comparison. The slowest detectors ($\sim 3,000$ fps), EMCCD cameras, have the highest quantum efficiency ($>90\%$) and intermediate precision for diffusion coefficients ($\sim 20\%$). Their time resolution is at the limit for detecting freely diffusing molecules for which only the tail of the correlation function can be captured, and an accurate determination of diffusion coefficient and concentration is not possible. However, to date they have been the detectors of choice and they are the only devices for which single molecule resolution has consistently been shown in *in vivo* measurements. We demonstrated that all cameras can measure absolute diffusion coefficients in accord with several independent techniques. The large amount of data created by these fast recording devices poses new problems for data treatment. First solutions are already available and further developments are expected in the near future, leading to faster correlation and data fitting. To date, especially reconfigurable hardware (FPGAs) seems to be a promising approach for real-time image processing, e. g., correlations. With these developments imaging FCS should become a valuable tool for biophysical research.

Acknowledgments

The project was supported by a NUS-BW (National University of Singapore / Baden-Württemberg, BW 2010-2) joint grant to J.L. and T.W, a doctoral scholarship by the National University of Singapore to A.P.S, a doctoral fellowship of the Helmholtz International Graduate School for Cancer Research to J.B., a doctoral fellowship of the Heidelberg Graduate School of Mathematical and Computational Methods for the Sciences to J.W.K. We thank Xilinx, San Jose, USA for donating the FPGAs on the LASP development board. The authors thank Christoph Garbe and Bernd Jähne for loaning us a *pco.edge* sCMOS camera and Christine Kräuter, as well as Wolfgang Mischler for support on it. The authors also thank Dynamic Analysis System Pte Ltd, Singapore for loan of a *SA-05* CMOS and Hamamatsu, Keybond, Singapore for loan of a *ORCA-Flash4.0* sCMOS.